Self-bound quark stars with a first-order two-to-three flavor phase transition

G. Teruya,^{1,*} G. Lugones,^{1,†} and A. G. Grunfeld^{2,3,‡}

¹ Universidade Federal do ABC, Centro de Ciências Naturais e Humanas,
 Avenida dos Estados 5001- Bangú, CEP 09210-580, Santo André, SP, Brazil.
 ² CONICET, Godoy Cruz 2290, Buenos Aires, Argentina
 ³ Departamento de Física, Comisión Nacional de Energía Atómica,
 Avenida del Libertador 8250, (1429) Buenos Aires, Argentina

We investigate self-bound quark stars in a flavor-dependent quark-mass density-dependent (QMDD) model with an excluded-volume correction. We chart the parameter space at zero pressure to identify self-bound regimes, including cases with a first-order $ud \to uds$ transition, and construct cold, β -equilibrated stellar sequences via the Tolman-Oppenheimer-Volkoff equations. The excluded-volume parameter κ controls the stiffness of the equation of state and thus masses, radii, tidal deformabilities, and moments of inertia. Intermediate repulsion typically reconciles $M_{\text{max}} \gtrsim 2\,M_{\odot}$ with current radius/tidal constraints, with hybrid self-bound objects more compatible than pure strange-quark stars. We identify three EOS-insensitive trends—dimensionless moment of inertia vs. compactness, tidal deformability vs. compactness, and gravitational vs. baryonic compactness—whose explicit κ -dependence largely disappears in dimensionless form (the first two being notably tighter than the third). These results provide model-guided priors and tools for discriminating between hadronic and self-bound EOS families with multimessenger data.

Keywords: Compact stars, Strange quark matter, Effective models for quark matter, Universal relations

I. INTRODUCTION

The standard description of neutron stars posits that they are composed of hadronic matter. Nevertheless, at sufficiently high baryon densities—such as those realized in neutron-star cores—strong-interaction dynamics may drive deconfinement and the emergence of quark degrees of freedom. Configurations hosting a quark-matter core are referred to as hybrid stars, whereas compact objects composed entirely of deconfined quark matter are known as strange quark stars when an absolutely stable, self-bound phase is realized.

Strange quark stars consist of strange quark matter (SQM), a self-bound deconfined phase of up, down, and strange quarks. The concept traces back to the seminal works of Itoh [1], Bodmer [2], and Witten [3], who proposed that the inclusion of the strange flavor can lower the energy per baryon below that of ordinary nuclear matter—the strange-matter hypothesis. In this picture, quark matter may constitute a stable phase with finite density at vanishing pressure. These considerations motivate a broader view of possible compact-star compositions and, in particular, prompt the question of whether self-bound phases might arise even in the absence of strangeness.

Although the inclusion of the strange degree of freedom often lowers the energy per baryon—favoring a three-flavor self-bound phase—the viability of self-bound two-flavor phases cannot be dismissed *a priori*. This has led to studies assessing whether two-flavor quark

matter (udQM)—composed of up and down quarks only—could be absolutely stable and thus self-bound under specific conditions [4]. Even if bulk udQM satisfies $E/A < 930 \,\mathrm{MeV}$ at T = P = 0, this is not, in itself, incompatible with the stability of ordinary nuclei: finite-size contributions from surface and curvature energies penalize small quark droplets. Within the multiple-reflection-expansion (MRE) framework, these finitesize corrections raise the energy per baryon by amounts that scale as $\propto \sigma A^{-1/3}$ and $\propto \gamma A^{-2/3}$, respectively, where A is the baryon number and σ (γ) denotes the surface (curvature) tension [5]. As a result, nuclei can remain absolutely stable even if bulk udQM is the ground state: the decay of a nucleus into a finite ud-quark drop must overcome the surface and curvature barriers. Quantitatively, these effects imply a minimum baryon number A_{\min} above which ud-quark matter droplets are favored, while hadronic matter is preferred below it; representative estimates yield $A_{\rm min} \gtrsim 300$ [4]. The precise threshold depends on the microphysics that controls σ and γ , for which effective-model calculations typically find sizable values, reinforcing the stabilizing role of finite-size terms [6, 7]. These considerations parallel the classical strange-matter arguments [3, 8] while emphasizing that stability in bulk does not automatically extend to finite lumps. In the stellar context, macroscopic self-bound configurations can circumvent finite-size penalties and may be realized as compact stars composed of deconfined quark matter, whereas in vacuum small ud droplets are unstable and hadronize.

Ab initio QCD at finite baryon density is presently out of reach: lattice calculations suffer from the sign problem, and perturbation theory is trustworthy only at asymptotically large densities. We therefore employ phenomenological equations of state (EOS). The MIT bag model encodes confinement through a bag constant B but

^{*} giulliano.teruya@aluno.ufabc.edu.br

 $^{^{\}dagger}$ german.lugones@ufabc.edu.br

[‡] ag.grunfeld@conicet.gov.ar

lacks dynamical chiral symmetry breaking/restoration, whereas the Nambu–Jona-Lasinio (NJL) model captures chiral dynamics via local four-fermion interactions yet does not confine [9–14]. This complementarity motivates a framework that incorporates, in a minimal and consistent way, both confinement and (effective) chiral behavior. In this work we adopt the quark-mass density–dependent (QMDD) model, wherein quark effective masses acquire a density dependence. Enforcing thermodynamic consistency introduces additional terms in the pressure that act as a confining contribution, while the masses approach their current values at high density, mimicking chiral restoration [15–17].

Two variants of the QMDD scheme were introduced in Ref. [15]: a flavor-blind ansatz, where the effective mass depends on the baryon number density, and a flavor-dependent ansatz, where each flavor's mass tracks its own particle number density. A comprehensive survey of the parameter space shows that, in the flavor-blind case, among parameter sets that yield absolute stability, the vanishing-pressure ground state is invariably three-flavor. In contrast, the flavor-dependent formulation admits a broad domain of parametrizations in which two-flavor matter is self-bound at zero pressure.

Most of our previous astrophysical applications employed the flavor-blind variant [16–18]. Here we focus on the flavor-dependent scheme. For parameter sets whose zero-pressure ground state is two-flavor, our preliminary calculations robustly produce a first-order $ud \rightarrow uds$ transition at higher pressures. This transition reshapes the EOS and permits compact configurations with an uds core enveloped by a ud mantle—a quark—quark "hybrid" that we term self-bound hybrid stars. In what follows we analyze the flavor-dependent model in detail and quantify the astrophysical consequences of the $ud \rightarrow uds$ transition.

The paper is organized as follows. Section II introduces the flavor-dependent QMDD framework, detailing the density-dependent mass ansatz and the excludedvolume prescription, and summarizes the resulting zerotemperature EOS. In Section III we delineate the stability window in the (a, C) plane and discuss causality bounds. Section IV presents the thermodynamics and phase structure—Gibbs energy per baryon, $p(\epsilon)$, and speed of sound—quantifying the two- to three-flavor transition (transition pressure and energy-density jump). In Section V we compute global stellar properties by solving the Tolman-Oppenheimer-Volkoff (TOV) equations and confront mass-radius, tidal deformability, and moment-of-inertia predictions with current multimessenger constraints. Section VI discusses EOS-insensitive ("universal") relations for self-bound stars. We conclude by summarizing the main results and their implications in Sec. VII. Technical details of the EOS construction and of the computations of Love numbers and the moment of inertia are collected in the Appendices A and В.

II. THE FLAVOR-DEPENDENT QMDD MODEL

We model cold quark matter as a gas of non-interacting quasiparticles of flavors u,d,s with effective masses M_i , supplemented by free electrons to ensure charge neutrality. Within the QMDD framework [15], interaction effects are encoded through density-dependent quark masses while the expressions for the energy density and the number densities retain the free-gas functional form. Specifically, the effective mass of each flavor is taken as

$$M_i = m_i + \frac{C}{n_i^{a/3}},\tag{1}$$

where $i \in \{u, d, s\}$, m_i is the (constant) current mass of flavor i, n_i is its number density, and C and a are flavor-independent parameters. Units are chosen so that M_i is in MeV when n_i is expressed in fm⁻³; throughout we adopt natural units with $\hbar = c = 1$. In contrast to our earlier "flavor-blind" formulation—where M_i depended only on the baryon number density—we employ here a flavor-dependent mass function $M_i(n_i)$.

The limiting behavior of Eq. (1) reproduces the expected qualitative features: as $n_i \to 0$, M_i diverges, suppressing quasiparticle excitations and thereby mimicking confinement; at asymptotically large densities, $M_i \to m_i$, providing a phenomenological realization of (effective) chiral restoration, particularly if $m_i = 0$. The exponent a can be related to a schematic interquark potential, $v(r) \propto r^a$, which controls how rapidly medium effects diminish with increasing density [15].

A natural way to encode repulsive interactions in the flavor-dependent QMDD model is to introduce a phenomenological excluded-volume correction that penalizes arbitrarily high local number densities, thereby stiffening the EOS at moderate and high densities [16]. Consistent with the flavor-dependent ansatz in Eq. (1), we take quarks of flavor i to reduce only the volume available to the same flavor (no interspecies reduction):

$$\tilde{V}_i = V - b(n_i) n_i V = V [1 - b(n_i) n_i],$$
 (2)

where $b(n_i)$ is the effective excluded volume per particle of flavor i (dimension of volume).

We set $b(n_i)$ via an ansatz that reflects the expected microphysical behavior of repulsive interactions: it yields a substantial per-particle excluded volume at low to intermediate densities and vanishes at high densities, consistent with asymptotic freedom. For consistency with the flavor-dependent mass prescription in Eq. (1), we also take the excluded volume per particle to be flavor dependent. Accordingly, in analogy with Refs. [15, 16], we adopt

$$b_i = \frac{\kappa}{n_i},\tag{3}$$

with $\kappa > 0$. Substituting this ansatz into Eq. (2) gives $\tilde{V}_i = V(1-\kappa)$ for i = u, d, s. Thus, in spite of the flavor-dependent parametrization, this ansatz leads to the same

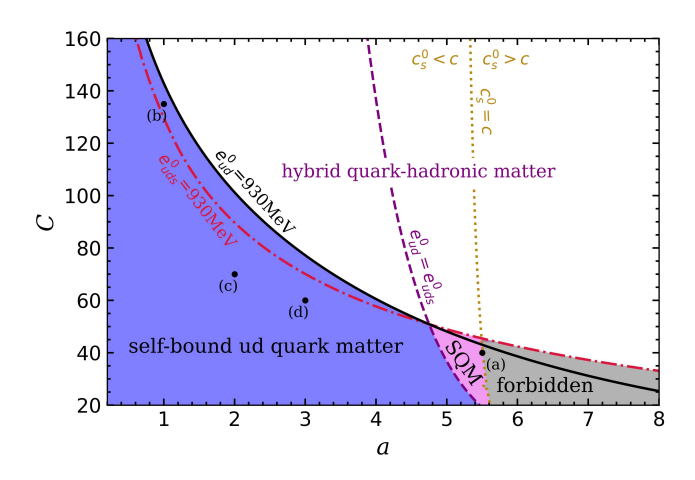


FIG. 1. Stability window of the flavor-dependent QMDD model in the (a,C) plane. The black (red) curve corresponds to $e^0_{ud} = 930\,\mathrm{MeV}$ ($e^0_{uds} = 930\,\mathrm{MeV}$); points lying below the respective curve yield self-bound ud (uds) matter at p=0. Points above both 930 MeV curves correspond to hybrid quark-hadronic matter. The indigo line marks $e^0_{ud} = e^0_{uds}$. The orange line indicates $c^0_s = c$; to its right the $p \to 0$ limit is acausal.

repulsive contribution across flavors, making the index i superfluous:

$$\tilde{V}_i \equiv \tilde{V} = V (1 - \kappa). \tag{4}$$

Substituting Eqs. (1) and (4) into the general flavor-dependent QMDD expressions of Ref. [16] yields the complete EOS. We collect the resulting formulas in Appendix A.

III. STABILITY WINDOW

At zero pressure, the energy per baryon

$$e^0 \equiv \frac{\epsilon}{n_B} \bigg|_{n=0}$$
, (5)

diagnoses whether quark matter is self-bound or only realized at high pressure. We take 930 MeV—the energy per nucleon of the most tightly bound nucleus, $^{62}{\rm Ni}$ —as the reference benchmark. If $e^0<930\,{\rm MeV}$, bulk hadronization is energetically disfavored and the matter is self-bound, so compact stars composed of it are pure quark stars. If $e^0>930\,{\rm MeV}$, quark matter is unbound at low pressure and the EOS is hybrid: hadronic at low pressure and deconfined only beyond a transition pressure, yielding hybrid stars with a quark core and a hadronic envelope.

Figure 1 shows the stability window of the flavor-dependent QMDD model in the (a,C) plane. The curves $e^0_{ud} = 930\,\mathrm{MeV}$ (black) and $e^0_{uds} = 930\,\mathrm{MeV}$ (red) delimit where two- and three-flavor matter, respectively, are self-bound at zero pressure: points lying below the former

TABLE I. Benchmark parameter sets used in this work. Labels (a)–(d) correspond to the points highlighted in Fig. 1. Model (a) is a pure strange–quark–matter case; models (b)–(d) are self–bound hybrid configurations featuring a two–to three–flavor $(ud \rightarrow uds)$ transition.

Label in Fig. 1	a	C
(a)	5.5	40
(b)	1	135
(c)	2	70
(d)	3	60

(latter) yield self-bound ud (uds) matter. Accordingly, self-bound ud quark matter (udQM) is realized when $e_{ud}^0 < e_{uds}^0$, whereas SQM occurs for parameter choices with $e^0_{uds} < e^0_{ud}$. Points above both 930 MeV curves correspond to hybrid EOSs—hadronic at low pressure and deconfined only beyond a transition pressure—leading to stars with a quark core and a hadronic envelope. An additional curve, $c_s^0 = c$, marks parameter choices for which the sound speed at zero pressure equals the speed of light. To its left, the EOS remains causal down to p=0; to its right, the $p\to 0$ limit becomes acausal $(c_s^0 > c)$, thereby excluding self-bound quark matter. Although the flavor-dependent QMDD model involves three parameters—a, C, and the excluded-volume parameter b—Ref. [16] shows that b does not modify the zero-pressure energy per baryon and thus does not affect the self-bound criterion. The stability region is therefore fully determined by (a, C).

The purple region in Fig. 1 corresponds to parameter choices for which bulk two-flavor quark matter would be more bound than the most tightly bound nucleus. As noted in the Introduction, this does not necessarily entail an instability of ordinary nuclei: finite-size costs from surface and curvature terms disfavor the formation of small ud droplets, so nuclear stability is preserved. The pink region (SQM) is likewise compatible with nuclear stability.

We analyze four benchmark points in the (a,C) plane, indicated by (a)–(d) in Fig. 1 and listed in Table I. Point (a), (a,C)=(5.5,40), lies in the SQM sector and serves as the reference strange–quark–matter EOS. Points (b) (1,135), (c) (2,70), and (d) (3,60) sample the self-bound ud domain and exemplify self-bound hybrid configurations in which a two– to three–flavor transition can occur. Unless stated otherwise, each benchmark is evaluated at several excluded–volume strengths, typically $\kappa=0,0.3,0.6$ [16]; the chosen κ values will be specified in the corresponding figures and captions.

IV. NUMERICAL RESULTS FOR THE EOS

Figure 2 displays the Gibbs free energy per baryon, $G/n_B = (\epsilon + p)/n_B$, for the parameter sets (a)–(d) defined in Fig. 1. For each (a,C), we show three representa-

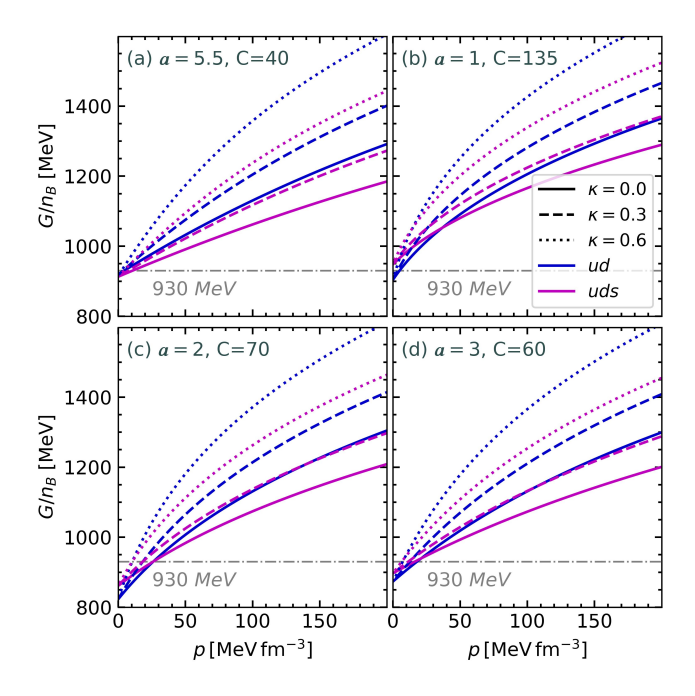


FIG. 2. Gibbs free energy per baryon for two- (ud) and three-flavor (uds) bulk quark matter. Curves correspond to the parameter sets (a)–(d) defined in Fig. 1 and three representative excluded-volume strengths κ (0, intermediate, high). At p=0, G/n_B is independent of κ . Crossings between ud and uds branches (when present) indicate a first-order $ud \to uds$ transition.

tive excluded-volume strengths κ (0, intermediate, high) as specified in Fig. 1. At p=0, G/n_B is independent of κ for both ud and uds matter. In all four cases, at least one of the two compositions satisfies $G/n_B < 930\,\mathrm{MeV}$ at zero pressure.

Two different scenarios emerge from these results. In Fig. 2(a), the uds branch lies below the corresponding ud branch at all pressures, identifying the strange-quarkmatter scenario in which three-flavor matter is favored throughout. By contrast, Figs. 2(b)-2(d) exhibit a scenario in which ud matter minimizes G/n_B at low pressure, whereas uds becomes energetically favored above a threshold. The ensuing $ud \rightarrow uds$ conversion is first order, as indicated by the crossing of the G/n_B branches and the accompanying discontinuity in energy density. The transition pressure depends on (a, C) and decreases monotonically with increasing κ ; the three panels illustrate representative cases in which the transition occurs at low, moderate, and high pressures. As discussed below, this systematic dependence on κ directly influences the extent of the three-flavor core in self-bound hybrid stars under different excluded-volume choices.

Figure 3 shows the total pressure p as a function of the energy density ϵ for the same parameter sets as in Fig. 2. In all cases, $p(\epsilon)$ crosses zero at a finite ϵ , reflecting the effective bag-like vacuum contribution generated by the density dependence of the quasiparticle masses in the QMDD model. For EOSs that undergo a first-order $ud \rightarrow$

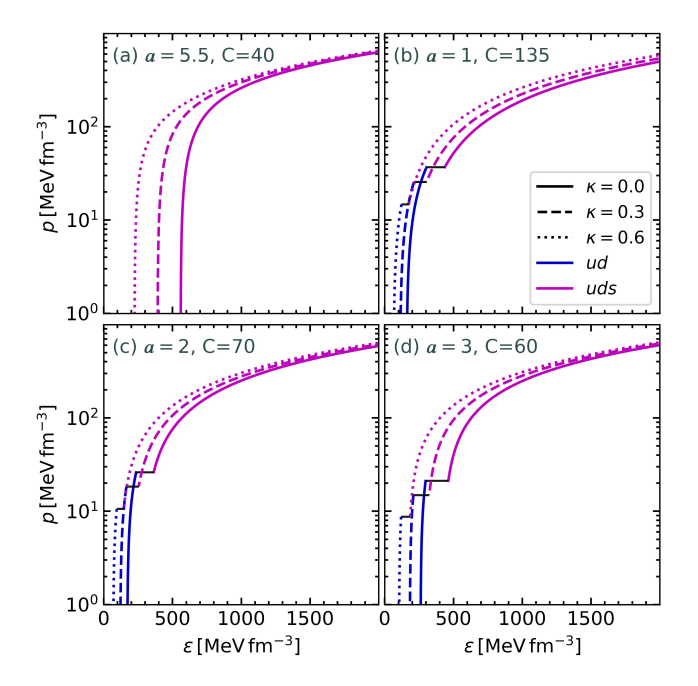


FIG. 3. Total pressure p versus energy density ϵ for the same parameter sets as Fig. 2. A constant-pressure plateau with a discontinuous jump in ϵ appears when a first-order $ud \rightarrow uds$ transition occurs; each curve crosses p=0 at finite ϵ .

uds transition, $p(\epsilon)$ exhibits a constant-pressure plateau accompanied by a discontinuous jump in ϵ (latent heat).

Table II summarizes the transition pressure $p_{\rm tr}$ and the associated energy densities. For fixed (a,C), increasing κ lowers $p_{\rm tr}$ and the energy-density discontinuity $\Delta \epsilon$; this monotonic dependence will be relevant for the stellar sequences discussed below.

Seidov [19] showed that, within general relativity, the onset of a first-order phase transition renders a spherically symmetric star unstable when the energy-density jump exceeds the critical value

$$\frac{\epsilon_{+}}{\epsilon_{-}} = \frac{3}{2} \left(1 + \frac{p_{\rm tr}}{\epsilon_{-}} \right),\tag{6}$$

where $p_{\rm tr}$ is the transition pressure and ϵ_- (ϵ_+) is the energy density just below (above) the transition. Table II lists $p_{\rm tr}$, ϵ_- , and ϵ_+ for all parameter sets considered here and, in the last column, the diagnostic ratio

$$q \equiv \frac{\epsilon_{+}/\epsilon_{-}}{\frac{3}{2}\left(1 + p_{\rm tr}/\epsilon_{-}\right)} \,. \tag{7}$$

All values lie in the range 0.85–0.97, i.e., below unity, so Seidov's instability criterion is not met. Hybrid configurations featuring a two- to three-flavor transition are therefore expected to remain dynamically stable; we confirm this in Sec. V by integrating the stellar structure equations and exhibiting stable branches in the mass–radius relation.

Table II further shows that, for fixed (a, C), $p_{\rm tr}$, ϵ_{-} ,

TABLE II. First-order $ud \to uds$ transition parameters for the flavor-dependent QMDD EOS. For each (a, C, κ) we list the transition pressure $p_{\rm tr}$, the energy densities just below/above the transition (ϵ_-, ϵ_+) , and the jump $\Delta \epsilon \equiv \epsilon_+ - \epsilon_-$. The last column reports the Seidov diagnostic $q \equiv (\epsilon_+/\epsilon_-)/\left[\frac{3}{2}(1+p_{\rm tr}/\epsilon_-)\right]$; values q < 1 indicate that the Seidov instability criterion is not met.

\overline{a}	C	κ	$p_{\rm tr}~({ m MeVfm^{-3}})$	$\epsilon_+ \; (\mathrm{MeV fm^{-3}})$	$\epsilon_{-} (\mathrm{MeV fm^{-3}})$	$\Delta \epsilon \; (\mathrm{MeV fm^{-3}})$	\overline{q}
1	135	0.0	36.8	436.7	303.8	132.9	0.855
1	135	0.3	25.8	305.8	212.7	93.0	0.855
1	135	0.6	14.7	174.8	121.7	53.1	0.854
2	70	0.0	26.2	363.4	235.8	127.6	0.925
2	70	0.3	18.4	254.5	165.2	89.3	0.924
2	70	0.6	10.6	145.6	94.5	51.1	0.924
3	60	0.0	21.1	462.5	297.5	165.0	0.968
3	60	0.3	14.9	324.0	208.3	115.7	0.968
3	60	0.6	8.7	185.6	119.2	66.4	0.967

and ϵ_+ vary appreciably with κ , whereas the combination in Eq. (6) is essentially insensitive to κ .

Figure 4 shows the sound speed c_s (in units of c) for the same parameter sets as in Fig. 2. At large baryon density n_B , c_s approaches the conformal limit $1/\sqrt{3}$. Each curve terminates at its zero-pressure point; the associated termination densities depend on κ . In Figs. 4(b)-4(d), the first-order $ud \rightarrow uds$ transition produces a constant-pressure interval with a discontinuous energy density, so c_s is undefined there and the interval is omitted.

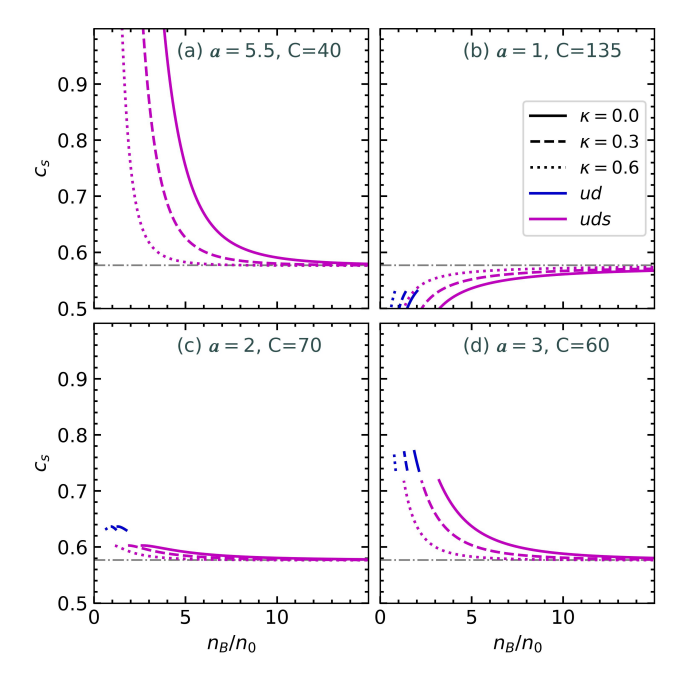


FIG. 4. Sound speed c_s (in units of c) versus baryon number density n_B for the same parameter sets as Fig. 2. The horizontal line marks the conformal limit $1/\sqrt{3}$; curves end at their zero-pressure points.

V. GLOBAL PROPERTIES OF HYBRID SELF-BOUND QUARK STARS

Having established the EOS properties across the chosen parameter sets, we now turn to the stellar structure they imply. Equilibrium configurations are obtained by integrating the general-relativistic TOV equations (see Appendix B1). As shown below, the global properties are highly sensitive to (a, C, κ) , giving rise to distinct classes of self-bound compact stars. The parameter-space regions delineated in Fig. 1 lead to qualitatively different sequences, summarized schematically in Fig. 5. Parameters in the SQM domain yield stars composed entirely of uds matter (configuration "4"). Parameters in the selfbound ud region ensure that the low-density end of the sequence (near $p \to 0$) remains two-flavor, producing the configurations labeled "1", "2", and "3" in Fig. 5 according to the central pressure p_c (the pressure at the stellar center). Specifically, if $p_c < p_{\rm tr}$ the star is purely twoflavor (configuration "1"), whereas for $p_c > p_{tr}$ a uds core forms within a ud mantle (configurations "2" and "3"), i.e., a self-bound hybrid star. For clarity, we denote by p_c^{max} the central pressure of the configuration that attains the maximum gravitational mass M_{max} along a given TOV sequence. Numerically, we do not encounter sequences with $p_c^{\text{max}} < p_{\text{tr}}$. For every self-bound choice in Fig. 1, the onset of the uds core precedes the maximummass configuration $(p_c^{\text{max}} \ge p_{\text{tr}})$, and the "purely twoflavor up to $M_{\rm max}$ " scenario is excluded by our solutions.

Using the same EOS parameter sets as above, we integrate the TOV equations and compute the stellar mass M, radius R, tidal deformability Λ , and moment of inertia I.

Figure 6 presents the mass–radius relations. Within each panel, line styles encode the excluded-volume strength κ (solid, dashed, dotted), following the same convention adopted in Fig. 2 (and subsequent figures). Increasing κ stiffens the EOS and raises $M_{\rm max}$. Panel 6(a) employs parameters in the SQM domain of Fig. 1, yielding sequences of pure three-flavor strange-quark stars (magenta). Panels 6(b)–6(d) use EOSs with a first-order $ud \to uds$ transition; the three parameter

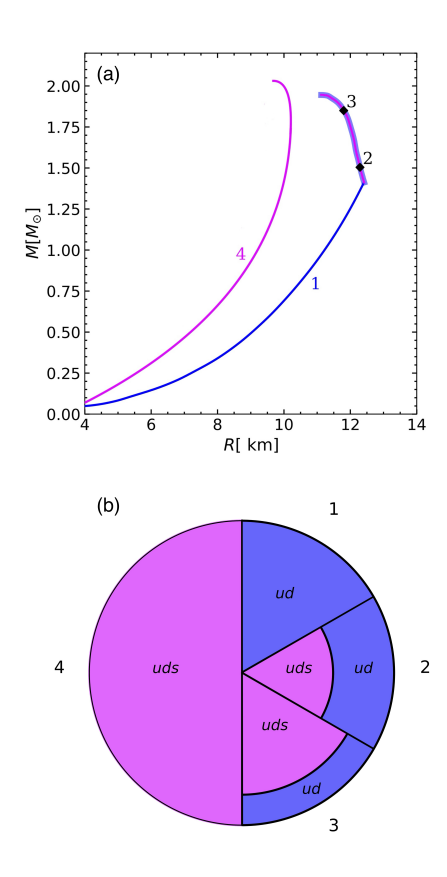


FIG. 5. (a) Schematic mass-radius diagram of self-bound stars. The magenta curve shows self-bound strange-quark-matter configurations, the blue curve shows self-bound ud stars, and the bicolor (magenta-blue) curve displays the sequence of self-bound hybrid stars analyzed in this work. (b) Representation of the internal composition of the models on the M-R curves in panel (a), indicating regions of uds matter (magenta) and ud matter (blue).

sets place the transition at low, intermediate, and high densities, respectively. For central pressures below the transition $(p_c < p_{\rm tr})$, the sequence consists of two-flavor stars (blue). Once $p_c > p_{\rm tr}$, a uds core forms within a ud mantle, producing self-bound hybrid stars (bicolor magenta/blue). The kink at $p_c = p_{\rm tr}$ marks the onset of the core.

Figure 6 confronts the mass–radius sequences with current astrophysical constraints. A clear dependence on the excluded-volume strength is evident. Models with $\kappa=0$ (solid) are too soft: their M-R curves fail to reach $2\,M_\odot$, underscoring the need for repulsive interactions in the quark sector. At the other extreme, $\kappa=0.6$ (dotted) produces very stiff EOSs. Although these sequences comfortably attain large maximum masses, they generally overpredict radii; in panels 6(b)-6(d) the curves lie on or above the upper edge of the PSR J0030+0451 and PSR J0740+6620 constraints. An exception occurs in

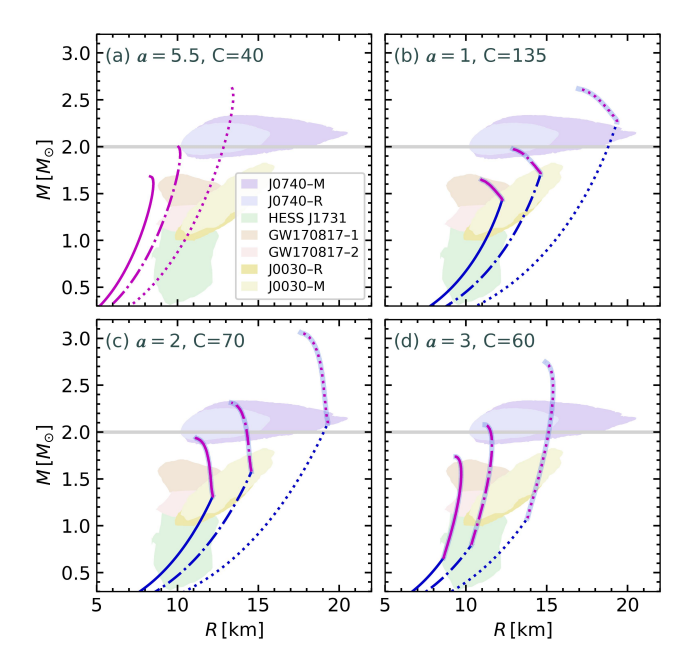


FIG. 6. Mass—radius relations for quark-star sequences computed with the EOS sets of Table I. Line styles encode the excluded-volume strength κ (solid, dashed, dotted), following the convention of Fig. 2. Colors indicate composition: magenta—pure uds (SQM); blue—pure ud; bicolor—self-bound hybrids with a uds core surrounded by a ud mantle. (a) Parameters in the SQM domain yield purely three-flavor sequences. (b)–(d) EOSs featuring a first-order $ud \rightarrow uds$ transition placed at low, intermediate, and high densities, respectively; the kink marks $p_c = p_{\rm tr}$. Increasing κ stiffens the EOS and raises $M_{\rm max}$. Shaded contours denote observational constraints from GW170817 [20–22], PSR J0030+0451 [23, 24], HESS J1731–347 [25], and PSR J0740+6620 [26, 27].

panel 6(a), where the pure SQM models with $\kappa=0.6$ are compatible with all bands, a marked improvement over $\kappa=0$ and 0.3. For the self-bound hybrid cases, the intermediate choice $\kappa=0.3$ (dashed) provides the best overall agreement, balancing the $2\,M_\odot$ requirement against radius constraints. Across panels 6(b)–6(d), the predicted $M_{\rm max}$ varies with the transition density: it is lower for both low and high transition densities and peaks for the intermediate case in panel 6(c).

Figure 7 displays the dimensionless tidal deformability Λ , which measures the induced quadrupole per unit external tidal field and provides a direct handle to confront the EOS with gravitational-wave observations (e.g., GW170817). We compute $\Lambda(M)$ for the same four EOS sets as in the preceding figures using the formalism summarized in Appendix B 2. The point with error bar marks the GW170817 constraint at $1.4\,M_{\odot}$. Two robust trends emerge. First, for any given EOS, Λ decreases monotonically with M as stars become more compact. Second, at fixed M, larger excluded volume (larger κ) yields larger Λ , reflecting EOS stiffening and the associated increase in radius. Quantitatively, at fixed mass one may write $\Lambda \simeq \frac{2}{3}\,k_2\,(R/M)^5$, so the strong compactness dependence

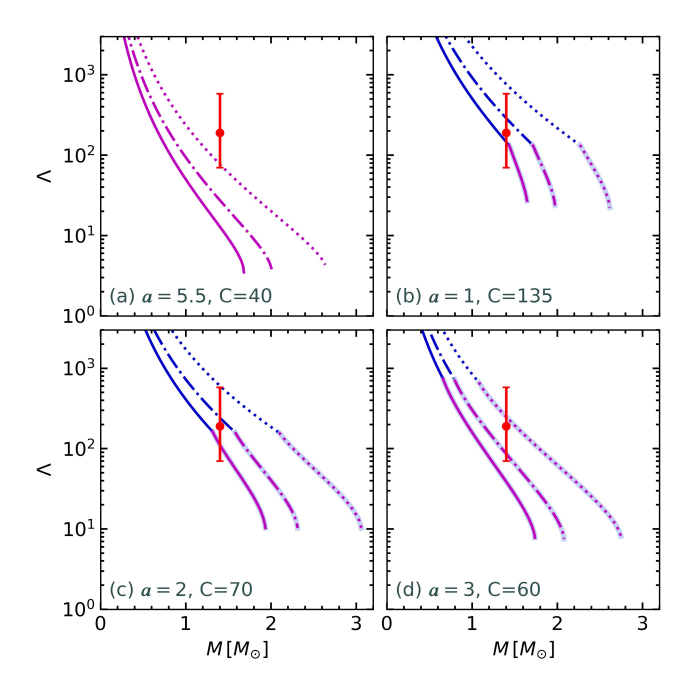


FIG. 7. Dimensionless tidal deformability Λ as a function of gravitational mass M for the same EOS sets used in Fig. 6. Line styles encode the excluded-volume strength κ (solid, dashed, dotted), following the convention of Fig. 2. (a) Pure strange–quark–star sequences; (b)–(d) self-bound hybrid-star sequences with the $ud \rightarrow uds$ transition placed at low, intermediate, and high densities, respectively. The point with error bar indicates the GW170817 constraint at $1.4\,M_{\odot}$ [20–22].

implies that even modest radius changes (few percent) can amplify Λ by tens of percent.

The observational implications differ for the two classes of models. For pure strange-quark stars [Fig. 7(a)], predicted deformabilities are generally too small to satisfy GW170817; only the stiffest case ($\kappa=0.6$) attains marginal consistency at $1.4\,M_\odot$. Self-bound hybrid stars [Figs.7(b)–7(d)] are, in general, consistent with the GW170817 constraint over a broad range of parameters. Two notable exceptions arise: (i) for high transition density combined with a large excluded volume ($\kappa=0.6$), the predicted Λ at $1.4, M_\odot$ is too large and lies outside the allowed GW170817 interval [Fig.7(b)]; and (ii) for low transition density with vanishing excluded volume ($\kappa=0.0$), the predicted Λ at $1.4, M_\odot$ is too small and likewise falls outside the allowed range [Fig. 7(d)].

We also compute the stellar moment of inertia I within the slow-rotation (Hartle–Thorne) approximation; the formalism is summarized in Appendix B3. Figure 8 shows I as a function of gravitational mass M for the models of the preceding figures, together with two hadronic benchmarks (SLy and APR).

The effect of the excluded-volume parameter is clear. At fixed M, larger κ yields larger I, reflecting EOS stiffening and the accompanying increase in radius. To leading order, I scales approximately as $I \sim MR^2$; thus the radius growth driven by repulsion translates directly into

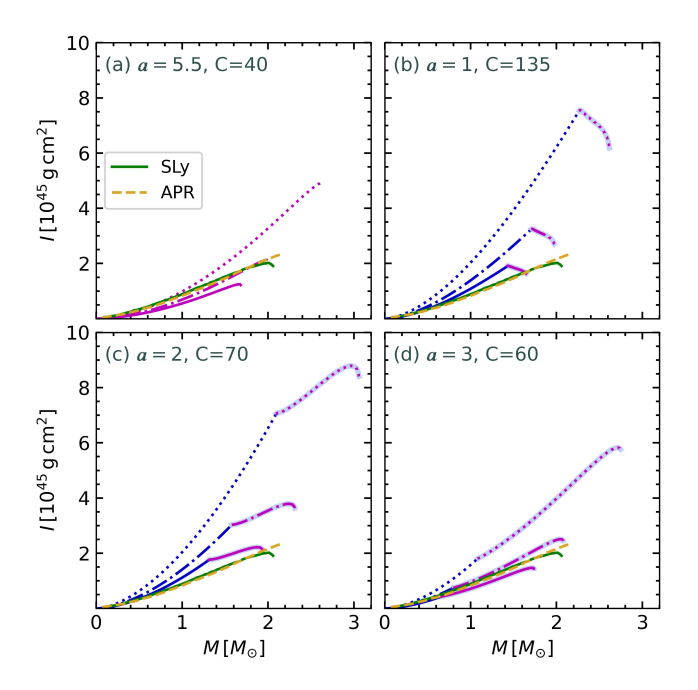


FIG. 8. Moment of inertia I as a function of gravitational mass M for the same EOS sets used in Fig. 6. (a) Pure strange–quark–star sequences; (b)–(d) self-bound hybrid-star sequences with the $ud \to uds$ transition placed at low, intermediate, and high densities, respectively. For reference, hadronic benchmarks (SLy and APR) are overplotted.

a higher moment of inertia. In Fig. 8(a), the pure SQM sequences track the hadronic fit rather closely, despite the different microphysics. For self-bound hybrid stars [Figs. 8(b)-8(d)], the appearance of a three-flavor (uds) core leaves a distinct imprint on I(M) at $p_c = p_{\rm tr}$. The behavior beyond the transition depends on the transition density. In the high-transition-density case [Fig. 8(b)], a "backbending" segment occurs: when a uds stellar core forms, I decreases even as M continues to increase, indicating pronounced central condensation. By contrast, for intermediate and low transition densities [Figs. 8(c)-8(d)] the hybrid branch remains monotonic, with I increasing with M up to nearly the maximum-mass configuration (very close to M_{max} a change of trend can occur). Only dynamically stable configurations are shown. Relative to SLy and APR, the $\kappa = 0$ quark matter sequences lie closest to the hadronic curves, whereas strong repulsion $(\kappa = 0.6)$ produces substantially larger I at a given M. These qualitative differences suggest that precision measurements of the moment of inertia (e.g., in double-pulsar systems) could help discriminate quark compositions and constrain the strength of repulsive interactions.

VI. UNIVERSAL RELATIONS

One of the most active directions in compact-star physics is the search for *universal relations*—functional

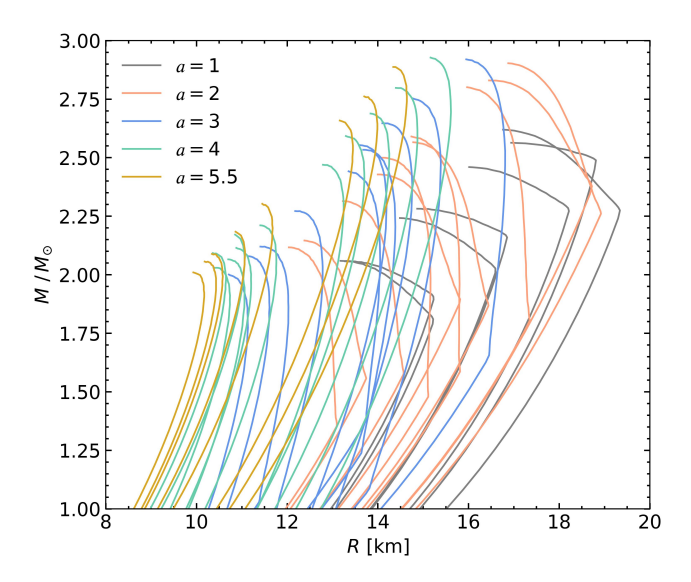


FIG. 9. Gravitational mass versus stellar radius for different choices of the EOS parameters (a, C, κ) . For each a, the parameter C was varied within its stability window (cf. Fig. 1) and the excluded-volume parameter was set to $\kappa \in \{0, 0.3, 0.6\}$.

correlations among macroscopic stellar quantities that depend only weakly on the underlying EOS. Such relations enable robust parameter inference: once some observables are measured, others can be estimated without detailed knowledge of the microphysics in the stellar core. Figure 9 displays the mass-radius sequences for a representative set of EOS constructed by fixing five values of the confinement parameter a and varying C, while the excluded-volume parameter is restricted to the three values $\kappa = 0.0, 0.3, 0.6$. We retain only those models whose maximum mass lies between $2 M_{\odot}$ and $3 M_{\odot}$, and whose maximum radius remains below 20 km. The lower bound enforces consistency with $\sim 2 M_{\odot}$ pulsars, whereas the upper bound together with the 20 km radius limit serve as conservative cuts to discard models with unrealistically large maximum masses and radii. This selected ensemble of models will be employed in the subsequent analysis of universal relations.

A. Dimensionless moment of inertia

Figure 10 shows the dimensionless moment of inertia, $\bar{I} \equiv I/M^3$, as a function of the compactness $\mathscr{C} \equiv M/R$. Despite the strong κ -dependence seen in individual M-R and M-I relations, its imprint is nearly washed out in the \bar{I} - \mathscr{C} plane: for fixed (a,C), the three κ tracks collapse to an excellent approximation onto a single curve. Moreover, the global trend across distinct (a,C) families is captured by a single fit (cyan dashed line). Remarkably, the same fitting form successfully described strange stars in previous work [18] based on the flavor-blind QMDD and vector MIT bag models. Its effectiveness here, for

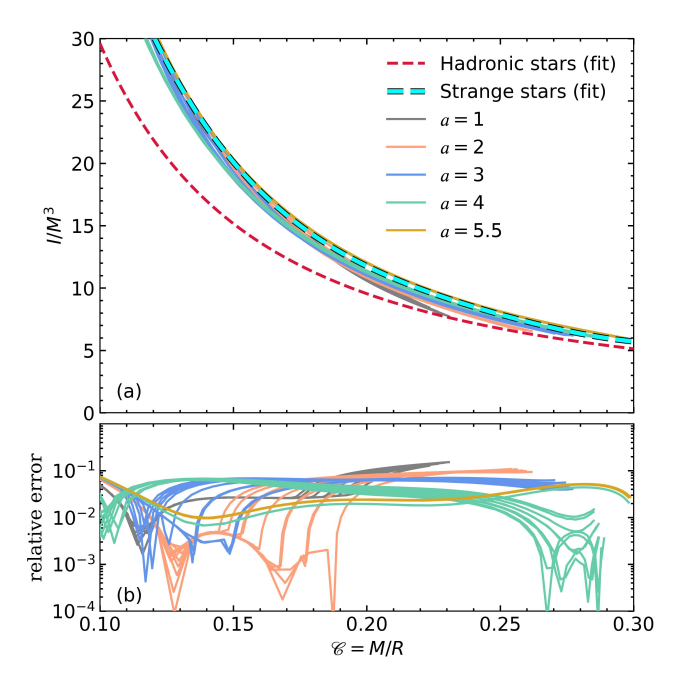


FIG. 10. (a) Dimensionless moment of inertia I/M_G^3 vs. compactness M_G/R for sequences with different values of a. Only EOSs with a maximum mass $2 \leq M_{\rm max}/M_{\odot} \leq 3$ are included. The dashed lines are the global fits for strange quark stars [18] and hadronic stars [28]. (b) Relative error, $\left|1-(I/M_G^3)_{\rm num}/(I/M_G^3)_{\rm fit}\right|$, with respect to the strange quark star fit.

stars with different EOS ingredients and internal compositions, underscores its high degree of universality.

A noteworthy exception occurs over an intermediate range of compactness, where sequences with small a (notably a=1 and a=2) depart more visibly from the fit, yielding the larger residuals shown in the lower panel. This behavior reflects the fact that for small a values, the onset of the hybrid branch causes a significant reduction in stellar radii. This, in turn, produces a sharp drop in compactness (cf. Fig. 6) without a comparable change in the dimensionless moment of inertia. Outside that interval, the scatter about the fit remains small and approximately uniform across the different (a,C) families.

It is worth emphasizing that the \bar{I} - \mathscr{C} relation for self-bound quark stars found here differs markedly from the purely hadronic relation of Breu and Rezzolla [28]. Consequently, a simultaneous measurement of M, R, and I would place a source at distinct loci in the \bar{I} - \mathscr{C} plane, offering a clean diagnostic to discriminate a self-bound quark star from a conventional hadronic star.

B. Tidal deformability versus compactness

Figure 11(a) displays an approximately universal relation between the dimensionless tidal deformability Λ and the compactness $\mathscr{C} = M/R$ for the self-bound quark-

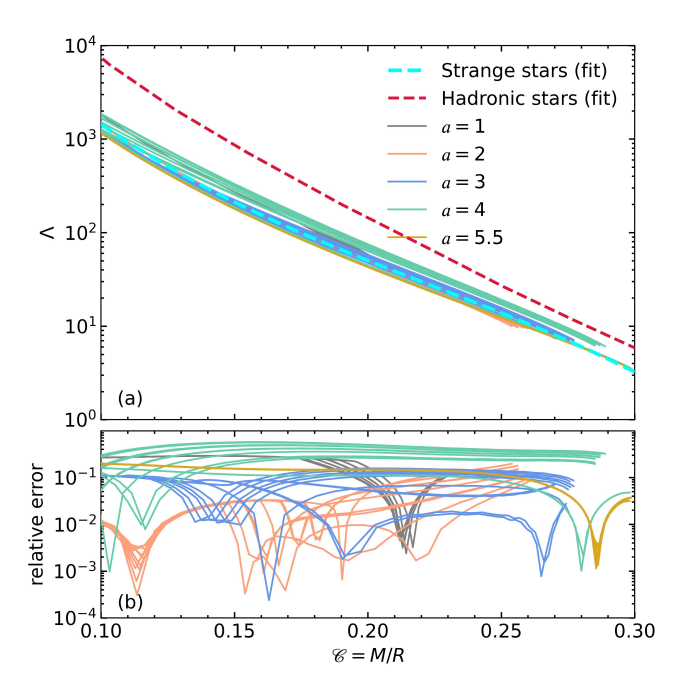


FIG. 11. Tidal deformability Λ as a function of the gravitational compactness $\mathscr{C}\equiv M_G/R$ for stellar sequences labeled by the parameter a. Panel (a): solid curves show the models; the cyan dashed line is the strange–quark–star fit [18] and the crimson dashed line is an empirical hadronic–star fit [28]. Panel (b): relative error with respect to the strange–quark–star fit, $|1-\Lambda/\Lambda_{\rm fit}^{\rm SQS}|$.

star models considered. In close analogy with the \bar{I} – $\mathscr C$ relation, the dependence on the excluded-volume parameter is negligible: for a fixed (a,C), sequences with $\kappa=0,0.3$, and 0.6 are practically indistinguishable and collapse onto a single curve. Moreover, curves from distinct (a,C) families cluster tightly around the strange-star fit (cyan dashed) obtained in Ref. [18] using the flavor-blind parametrization. The fidelity of this universal behavior is quantified in Fig. 11(b), which shows the relative deviation from the fit.

For reference, Fig. 11(a) also includes a representative hadronic fit (crimson dashed). The two relations remain clearly distinct over the full compactness range: at fixed \mathscr{C} , hadronic stars exhibit systematically larger Λ than self-bound quark stars. This offset has a clear physical origin. Self-bound objects possess a finite surface density and more homogeneous interiors, which yield smaller Love numbers k_2 ; because $\Lambda \propto k_2 \mathscr{C}^{-5}$, the reduced k_2 directly translates into a smaller tidal deformability.

In summary: (i) the Λ – $\mathscr C$ relation is effectively insensitive to κ ; (ii) the strange-star fit from Ref. [18]—previously shown to describe vMIT + QMDD flavor-blind data—also captures models with internal $ud \to uds$ transitions; and (iii) the quark-star and hadronic relations are well separated, offering an observational discriminator across the entire compactness range explored.

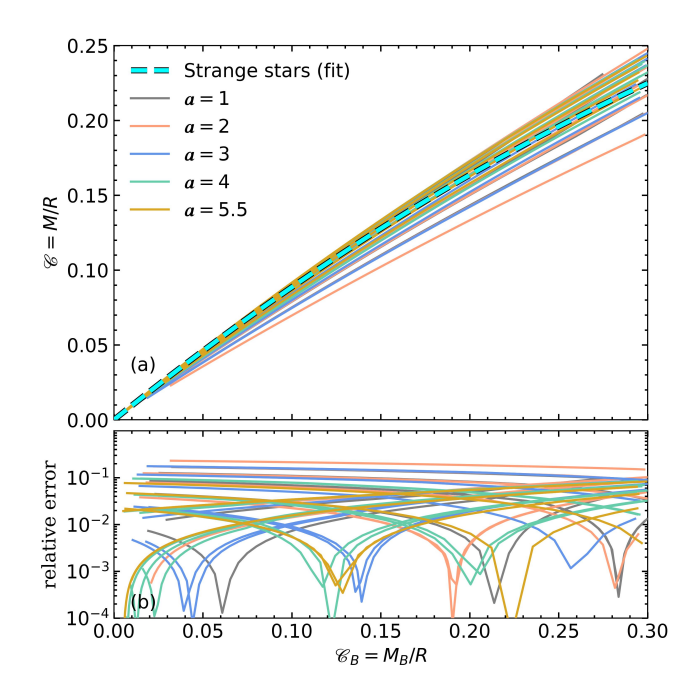


FIG. 12. Gravitational compactness $\mathscr C$ versus baryonic compactness $\mathscr C_B$ for stellar sequences labeled by the parameter a (colors as in the legend). Panel (a): solid curves show the models, while the cyan dashed line is the strange–quark–star fit [18]. Panel (b): relative error with respect to the fit, $|1-\mathscr C/\mathscr C^{\mathrm{fit}}|$.

C. Gravitational versus baryonic compactness

Figure 12(a) exhibits an approximately universal correlation for self-bound stars between the gravitational compactness $\mathscr{C} \equiv M/R$ and the baryonic compactness $\mathscr{C}_B \equiv M_B/R$, where the latter is computed from the conserved baryon number as given in Eqs. (B6) and (B7). For a fixed (a,C) family the three κ sequences collapse onto essentially the same path, mirroring our findings for the \bar{I} - \mathscr{C} and Λ - \mathscr{C} relations. Tracks from distinct (a,C) families cluster around a single global law, albeit with a larger dispersion than in the other universal relations, indicating an approximately EOS-insensitive mapping between \mathscr{C}_B and \mathscr{C} .

To quantify this behavior, Fig. 12(a) includes the analytic fit introduced in Ref. [18], which accurately describes the combined vMIT and flavor-blind QMDD strange-star dataset. The accuracy is assessed in Fig. 12(b), which presents the relative deviation from that fit. For many parameterizations the scatter remains below the percent level, whereas for others it can reach up to $\sim 20\%$, mirroring the residual patterns seen in the \bar{I} - \mathscr{C} and Λ - \mathscr{C} cases.

In summary, Fig. 12 shows that: (i) self-bound stars follow a \mathscr{C} - \mathscr{C}_B correlation broadly consistent with our previously proposed fit; (ii) residuals are typically below the few-percent level across much of the explored range; and (iii) the $\mathscr{C} \leftrightarrow \mathscr{C}_B$ mapping provides a prac-

tical leading-order approximation to estimate M_B and binding energies from (M, R) (or \mathscr{C}).

VII. CONCLUSIONS

We have investigated the macroscopic properties of self–bound quark stars within a flavor–dependent QMDD framework with an excluded–volume correction, exploring both SQM and self–bound two–flavor matter that undergoes a first–order transition to three flavors at high pressure. First, we mapped the (a,C) parameter space at zero pressure to identify the parametrizations that produce self–bound matter, including those that undergo a first–order $ud \rightarrow uds$ transition. We then computed cold, β –equilibrated, charge–neutral stellar sequences by solving the TOV equations. The principal outcomes are as follows.

- (i) Phase structure and stability. For broad regions of (a, C), the flavor-dependent EOS exhibits a first-order $ud \to uds$ phase transition whose transition pressure decreases with increasing excluded-volume parameter κ . The associated energy-density jumps satisfy Seidov's bound below the instability threshold. Quantitatively, the ratio $(\epsilon_+/\epsilon_-)/\left[\frac{3}{2}(1+p_{\rm tr}/\epsilon_-)\right]$ lies in the range 0.85–0.97 for all cases considered and is essentially insensitive to κ at fixed (a, C) (cf. Eq. (6) and Table II). In line with this expectation, the hybrid self-bound configurations occupy stable branches of the mass-radius relation.
- (ii) Global stellar properties and observational constraints. The parameter κ has a strong and systematic impact on the stiffness of the EOS and therefore on masses, radii, tidal deformabilities, and moments of inertia. In the absence of excluded volume ($\kappa = 0$), maximum masses tend to undershoot the $\sim 2\,M_{\odot}$ constraint, whereas large κ values can overshoot radius bounds at canonical masses. Intermediate repulsion (e.g., $\kappa \approx 0.3$) often reconciles $M_{\rm max} \gtrsim 2\,M_{\odot}$ with recent NICER inferences [23, 24, 26, 27] and the compact object in HESS J1731-347 [25]. Consistent with our detailed results, $\Lambda(M)$ decreases steeply with mass and increases with κ ; self-bound hybrid stars are typically more compatible with the GW170817 constraint at $1.4 M_{\odot}$ than pure SQM stars, the latter requiring comparatively strong repulsion to approach the observed range.
- (iii) Universal relations. Three EOS-insensitive trends emerge: (a) the dimensionless moment of inertia $\bar{I} \equiv I/M_G^3$ versus compactness \mathscr{C} , (b) the tidal deformability Λ versus \mathscr{C} , and (c) the gravitational versus baryonic compactness, $\mathscr{C}-\mathscr{C}_B$. In all cases, the explicit dependence on κ largely disappears once the relations are expressed in di-

mensionless form. These relations follow the flavor–blind strange–quark–star fits reported previously [18], with typical residuals below the percent level and larger deviations up to ~ 10 –20% for a few a families (where the phase transition reshapes the stellar structure). The $\mathscr{C}-\mathscr{C}_B$ mapping is less tight. Self-bound hybrid stars remain close to the universal relations but exhibit slightly larger departures than strange quark stars, due to the change in stiffness across the two- to three-flavor EOS transition. Because the onset of this transition varies among parameter sets, the effect manifests as a spread of curves for some parametrizations.

(iv) Quark-hadron discrimination. For fixed compactness, self-bound stars generically yield smaller Love numbers and smaller Λ than hadronic stars, and their \bar{I} - \mathscr{C} curves also differ from hadronic fits. Hence, joint constraints on (M_G,R) together with either I or Λ can help discriminate self-bound quark stars from purely hadronic stars. We also find that models with $\kappa=0$ yield I(M) closer to hadronic benchmarks (SLy, APR), whereas increasing κ systematically raises I—a trend that future moment-of-inertia measurements could exploit.

Overall, the flavor–dependent QMDD model with excluded volume accommodates both SQM stars and self–bound hybrid stars compatible with current multimessenger constraints, and it exhibits EOS–insensitive trends that are useful for inference. The relations involving \bar{I} and Λ are comparatively tight, whereas the $\mathscr{C}-\mathscr{C}_B$ mapping, though practical for first–order estimates of baryonic masses and binding energies, carries larger model–dependent scatter in specific regions of parameter space.

Taken together, these results provide a minimal and coherent baseline for interpreting self-bound configurations within a simple, transparent framework. The dimensionless relations can be folded into inference pipelines either as informative priors or as independent consistency checks, by comparing the quantities inferred from data with the values predicted by our fits.

ACKNOWLEDGEMENTS

GL acknowledges the financial support from the Brazilian agency CNPq (grant 316844/2021-7). AGG acknowledges the financial support from CONICET under Grant No. PIP 22-24 11220210100150CO, ANPCyT (Argentina) under Grant PICT20-01847, and the National University of La Plata (Argentina), Project No. X960.

Appendix A: The EOS

EOS for pointlike quasiparticles

At T=0, the energy density, pressure, and chemical potentials of *pointlike* (pl) quasiparticles are written in terms of the number densities n_i as

$$\epsilon_{\rm pl} = \sum_{i} \epsilon_{{\rm pl},i} + \epsilon_e = \sum_{i} g M_i^4 \chi(x_i) + \epsilon_e,$$
 (A1)

$$p_{\rm pl} = \sum_{i} p_{{\rm pl},i} + p_e = \sum_{i} (gM_i^4 \phi(x_i) - B_i) + p_e, (A2)$$

$$\mu_{\text{pl},i} = M_i \sqrt{x_i^2 + 1} - \frac{B_i}{n_i}.$$
 (A3)

Here q denotes the spin-color degeneracy (for quarks q =6), M_i is the effective quasiparticle mass for flavor i, and the quantity B_i is an effective bag term arising from the density dependence of M_i :

$$-B_i = g \beta(x_i) M_i^3 n_i \frac{\partial M_i}{\partial n_i}.$$
 (A4)

The dimensionless Fermi momentum is

$$x_i = \frac{1}{M_i} \left(\frac{6\pi^2 n_i}{g} \right)^{1/3},$$
 (A5)

and

$$\chi(x) = \frac{x\sqrt{1+x^2}(2x^2+1) - \sinh^{-1}x}{16\pi^2},$$
 (A6)

$$\phi(x) = \frac{x\sqrt{1+x^2}(2x^2-3) + 3\sinh^{-1}x}{48\pi^2}, \quad (A7)$$

$$\beta(x) = \frac{x\sqrt{1+x^2} - \sinh^{-1}x}{4\pi^2}. \quad (A8)$$

$$\beta(x) = \frac{x\sqrt{1+x^2} - \sinh^{-1} x}{4\pi^2}.$$
 (A8)

Electron contributions (ϵ_e, p_e) follow the usual zerotemperature expressions with q=2.

Excluded-volume effects

We incorporate short-range repulsion via an excluded-volume prescription in the T=0 Helmholtz representation, following Refs. [16, 17]. Consistent with the flavor-dependent mass model, we take

$$b_i = \frac{\kappa}{n_i}, \quad \kappa > 0,$$
 (A9)

so that each flavor removes a fraction $b_i n_i = \kappa$ per unit volume. Thus the available volume fraction is flavor-independent,

$$q \equiv 1 - \kappa, \qquad 0 < q \le 1, \tag{A10}$$

even though the ansatz is flavor-dependent through n_i . In practice, the excluded-volume mapping amounts to evaluating the point-like quark expressions at rescaled densities $\tilde{n}_i \equiv n_i/q$ and multiplying the quark-sector thermodynamic quantities by q (the electron sector is left unchanged). The excluded-volume corrected EOS reads

$$\epsilon = \sum_{i} q \epsilon_{\text{pl},i} + \epsilon_{e} = \sum_{i} q g \tilde{M}_{i}^{4} \chi \left(\tilde{x}_{i} \right) + \epsilon_{e}, \tag{A11}$$

$$p = \sum_{i} q p_{\text{pl},i} + p_e = \sum_{i} q(g \tilde{M}_i^4 \phi(\tilde{x}_i) - \tilde{B}_i) + p_e, \text{ (A12)}$$

$$\mu_i = \tilde{M}_i \sqrt{\tilde{x}_i^2 + 1} - \frac{\tilde{B}_i}{\tilde{n}_i}, \tag{A13}$$

with

$$\tilde{n}_i = n_i/q, \tag{A14}$$

$$\tilde{M}_i = M_i(\tilde{n}_i), \qquad (A15)$$

$$\tilde{x}_i = \frac{1}{\tilde{M}_i} \left[\frac{6\pi^2 (n_i/q)}{g} \right]^{1/3},$$
 (A16)

$$-\tilde{B}_{i} = g\beta(\tilde{x}_{i})\tilde{M}_{i}^{3}\tilde{n}_{i}\frac{\partial\tilde{M}_{i}}{\partial\tilde{n}_{i}}.$$
 (A17)

Thermodynamic consistency is preserved by construction, and the point–like limit is recovered for $\kappa \to 0$ $(q \to 1)$. We note that the Gibbs free energy per baryon at p=0 is insensitive to κ in this construction, in agreement with the results shown in the main text.

Compact-star conditions 3.

For cold, catalyzed matter in compact stars we impose local charge neutrality and β equilibrium (with freely streaming neutrinos). The chemical-equilibrium conditions read

$$\mu_d = \mu_u + \mu_e, \qquad \mu_s = \mu_d, \tag{A18}$$

with $\mu_{\nu_e} = 0$, while charge neutrality requires

$$\frac{2}{3}n_u - \frac{1}{3}n_d - \frac{1}{3}n_s - n_e = 0. \tag{A19}$$

(Throughout, we use natural units $\hbar = c = 1$.)

Appendix B: Stellar structure

The EOS developed above is used to determine global properties of self-bound compact stars—mass-radius relations, tidal deformabilities, and (in the slow-rotation regime) moments of inertia. For completeness, we summarize here the field equations and integrals needed for these calculations. Throughout this appendix we work in geometrized units, G = c = 1.

TOV equations

We assume a static, spherically symmetric spacetime with line element

$$ds^{2} = e^{2\nu(r)}dt^{2} - e^{2\lambda(r)}dr^{2} - r^{2}(d\theta^{2} + \sin^{2}\theta \,d\phi^{2}),$$
 (B1)

and a perfect–fluid stress–energy tensor characterized by energy density $\epsilon(r)$ and pressure p(r). Hydrostatic equilibrium is governed by the TOV equations

$$\frac{dp}{dr} = -\frac{\left[\epsilon(r) + p(r)\right]\left[m(r) + 4\pi r^3 p(r)\right]}{r\left[r - 2m(r)\right]},$$
 (B2)

$$\frac{dm}{dr} = 4\pi r^2 \epsilon(r) \,, \tag{B3}$$

$$\frac{d\nu}{dr} = \frac{m(r) + 4\pi r^3 p(r)}{r \lceil r - 2m(r) \rceil},$$
(B4)

where m(r) is the enclosed gravitational mass. Regularity at the center requires m(0) = 0 and $p(0) = p_c$ (the latter sets the stellar model). The stellar surface r = R is defined by p(R) = 0, and the gravitational mass is

$$M \equiv m(R).$$
 (B5)

Matching to the exterior Schwarzschild solution fixes $e^{2\nu(R)}=1-2M/R$. The compactness used in the main text is $\mathscr{C}\equiv M/R$.

Let $n_B(r)$ denote the proper baryon number density. The total baryon number is

$$A_B = \int_0^R 4\pi r^2 n_B(r) \left(1 - \frac{2m(r)}{r}\right)^{-1/2} dr, \quad (B6)$$

and the baryonic mass is $M_B \equiv m_B A_B$, where m_B is a chosen baryon rest mass (often taken as the neutron mass m_n). For orientation, a canonical compact star with $M \simeq 1.4 \, M_{\odot}$ typically has $A_B \simeq 1.7 \times 10^{57}$, implying

$$M_B = A_B m_n \simeq 0.842 A_{B57} M_{\odot}, \quad A_{B57} \equiv \frac{A_B}{10^{57}}.$$
 (B7)

In the absence of mass accretion or mass loss, A_B (and hence M_B) is conserved along quasi-static evolutions.

2. Dimensionless tidal deformability

During the inspiral of a binary neutron–star system, the external quadrupolar tidal field \mathcal{E}_{ij} induces a mass–quadrupole moment Q_{ij} in each star. In linear response one writes

$$Q_{ij} = -\lambda \mathcal{E}_{ij} = -\Lambda M^5 \mathcal{E}_{ij}, \tag{B8}$$

where λ is the (dimensionful) tidal deformability, M is the gravitational mass, and $\Lambda \equiv \lambda/M^5$ is the dimensionless tidal deformability quoted in the main text. It is given by

$$\Lambda = \frac{2}{3}k_2\mathscr{C}^{-5},\tag{B9}$$

being k_2 the (quadrupolar) Love number.

Following the standard relativistic perturbation formalism, k_2 can be expressed in terms of $\mathscr C$ and the surface

value $y_R \equiv y(r = R)$ of the first order metric perturbation function y(r):

$$k_2 = \frac{8}{5} \mathscr{C}^5 (1 - 2\mathscr{C})^2 \frac{\left[2 - y_R + 2\mathscr{C}(y_R - 1)\right]}{\mathscr{D}},$$
 (B10)

with

$$\mathcal{D} = 2\mathscr{C} \left[6 - 3y_R + 3\mathscr{C}(5y_R - 8) \right]$$

$$+ 4\mathscr{C}^3 \left[13 - 11y_R + \mathscr{C}(3y_R - 2) + 2\mathscr{C}^2(1 + y_R) \right]$$

$$+ 3(1 - 2\mathscr{C})^2 \left[2 - y_R + 2\mathscr{C}(y_R - 1) \right] \ln(1 - 2\mathscr{C}).$$
(B11)

The function y(r) obeys the first-order ODE

$$r\frac{dy}{dr} + y^2 + yF(r) + r^2Q(r) = 0,$$
 (B12)

with coefficients

$$F(r) = \frac{1 - 4\pi r^2 [\epsilon(r) - p(r)]}{1 - 2m(r)/r},$$
(B13)

$$Q(r) = \frac{4\pi \left[5\epsilon(r) + 9p(r) + \frac{\epsilon(r) + p(r)}{c_s^2(r)} - \frac{6}{4\pi r^2} \right]}{1 - 2m(r)/r} - \frac{4m^2(r)}{r^4} \frac{\left[1 + 4\pi r^3 p(r) / m(r) \right]^2}{\left[1 - 2m(r) / r \right]^2},$$
(B14)

where $c_s^2 \equiv dp/d\epsilon$, and m(r), p(r), $\epsilon(r)$ are the TOV solutions from Eqs. (B2)–(B4). Regularity at the center sets y(0) = 2. The Love number k_2 and hence Λ follow by integrating (B12) together with the TOV equations up to r = R. For additional details, see Ref. [29].

Junction conditions at a first-order interface. When a sharp $(ud \to uds)$ first-order transition occurs at pressure $p_{\rm tr}$, located at radius $r_{\rm tr}$ defined by $p(r_{\rm tr}) = p_{\rm tr}$, the stellar solution must satisfy the Israel-Darmois junction conditions across the infinitesimal interface (assumed free of surface stresses). In static spherical symmetry these reduce to continuity of the induced metric and extrinsic curvature, which in practice implies continuity of the metric functions (hence of m and ν) and of the pressure, while allowing a jump of the energy density from ϵ_- to ϵ_+ (with $\Delta \epsilon \equiv \epsilon_+ - \epsilon_- > 0$). For the tidal sector, the first-order ODE for y(r) must be matched by enforcing the standard jump obtained by integrating the perturbation equation across the density discontinuity $(\delta \to 0)$ [29, 30]:

$$y(r_{\rm tr} + \delta) = y(r_{\rm tr} - \delta) - \frac{4\pi r_{\rm tr}^3 \Delta \epsilon}{m(r_{\rm tr}) + 4\pi r_{\rm tr}^3 p_{\rm tr}},$$
 (B15)

after which the integration proceeds to the surface to compute k_2 and Λ . This prescription guarantees continuity of the physical (gauge–invariant) metric perturbations across the interface and a well–posed Love number.

3. Moment of inertia for slow rigid rotation

We evaluate the stellar moment of inertia within the slow–rotation (Hartle–Thorne) framework, restricting attention to uniform rotation with angular frequency Ω as measured at infinity [31]. To first order in Ω , the total angular momentum is $J = \Omega I$, so that

$$I = \frac{J}{\Omega}, \qquad (B16)$$

and I is determined entirely by the mass—energy distribution and the spacetime of the corresponding nonrotating configuration.

It is convenient to compute I by integrating a first-order equation for the cumulative (enclosed) moment of inertia $\mathscr{I}(r)$,

$$\frac{d\mathscr{I}}{dr} = \frac{8\pi}{3} r^4 \epsilon \left(1 + \frac{p}{\epsilon}\right) \left(1 - \frac{5}{2} \frac{\mathscr{I}}{r^3} + \frac{\mathscr{I}^2}{r^6}\right) \left(1 - \frac{2m}{r}\right)^{-1},\tag{B17}$$

where m(r) is the mass function, and p(r) and $\epsilon(r)$ are supplied by the TOV solution (Sec. B1). Regularity at the center imposes $\mathscr{I}(0) = 0$, and the stellar moment of inertia follows as

$$I = \mathscr{I}(R), \tag{B18}$$

with R the radius where p(R) = 0. This formulation is equivalent to the standard computation based on the frame-dragging function $\bar{\omega}(r) = \Omega - \omega(r)$ and its exterior matching; see, e.g., Refs. [32, 33].

Remark on first-order phase transitions. Across an infinitesimal interface at $r_{\rm tr}$, one integrates Eq. (B17) on each side and impose continuity of the angular-momentum flux. In the equivalent frame-dragging formulation this means $\bar{\omega}$ and $r^4j\bar{\omega}'$ (with $j\equiv e^{-(\nu+\lambda)/2}$) are continuous at $r_{\rm tr}$. Hence $\mathscr{I}(r)$ is continuous and $I=\mathscr{I}(R)$ is well defined.

- N. Itoh, Hydrostatic Equilibrium of Hypothetical Quark Stars, Prog. Theor. Phys. 44, 291 (1970).
- [2] A. R. Bodmer, Collapsed nuclei, Phys. Rev. D 4, 1601 (1971).
- [3] E. Witten, Cosmic Separation of Phases, Phys. Rev. D 30, 272 (1984).
- [4] B. Holdom, J. Ren, and C. Zhang, Quark matter may not be strange, Phys. Rev. Lett. 120, 222001 (2018), arXiv:1707.06610 [hep-ph].
- [5] J. Madsen, Physics and astrophysics of strange quark matter, Lect. Notes Phys. 516, 162 (1999), arXiv:astroph/9809032.
- [6] G. Lugones, A. G. Grunfeld, and M. Al Ajmi, Surface tension and curvature energy of quark matter in the Nambu-Jona-Lasinio model, Phys. Rev. C 88, 045803 (2013), arXiv:1308.1452 [hep-ph].
- [7] G. Lugones and A. G. Grunfeld, Surface and curvature properties of charged strangelets in compact objects, Phys. Rev. C 103, 035813 (2021), arXiv:2010.06098 [nucl-th].
- [8] E. Farhi and R. L. Jaffe, Strange Matter, Phys. Rev. D 30, 2379 (1984).
- [9] L. L. Lopes, C. Biesdorf, and D. e. P. Menezes, Modified MIT bag Models—part I: Thermodynamic consistency, stability windows and symmetry group, Phys. Scripta 96, 065303 (2021), arXiv:2005.13136 [hep-ph].
- [10] L. L. Lopes, C. Biesdorf, K. D. Marquez, and D. P. Menezes, Modified MIT Bag Models part II: QCD phase diagram and hot quark stars, Phys. Scripta 96, 065302 (2021), arXiv:2009.13552 [hep-ph].
- [11] G. Lugones and A. G. Grunfeld, Vector interactions inhibit quark-hadron mixed phases in neutron stars, Phys. Rev. D 104, L101301 (2021), arXiv:2109.01749 [nucl-th].
- [12] Y. Nambu and G. Jona-Lasinio, Dynamical Model of Elementary Particles Based on an Analogy with Superconductivity. 1., Phys. Rev. 122, 345 (1961).

- [13] Y. Nambu and G. Jona-Lasinio, Dynamical model of elementary particles based on an analogy with superconductivity. II., Phys. Rev. 124, 246 (1961).
- [14] M. Buballa and M. Oertel, Strange quark matter with dynamically generated quark masses, Phys. Lett. B 457, 261 (1999), arXiv:hep-ph/9810529.
- [15] G. Lugones and A. G. Grunfeld, Cold dense quark matter with phenomenological medium effects: A self-consistent formulation of the quark-mass density-dependent model, Phys. Rev. D 107, 043025 (2023), arXiv:2209.03455 [nucl-th].
- [16] G. Lugones and A. G. Grunfeld, Excluded volume effects in the quark-mass density-dependent model: Implications for the equation of state and compact star structure, Phys. Rev. D 109, 063025 (2024), arXiv:2312.16095 [nucl-th].
- [17] G. Lugones and A. G. Grunfeld, Strange Quark Stars: The Role of Excluded Volume Effects, Universe 10, 233 (2024), arXiv:2405.18249 [nucl-th].
- [18] G. Lugones and A. G. Grunfeld, Scaling and universality in strange quark stars, arXiv preprint arXiv:2503.11515 (2025).
- [19] Z. F. Seidov, The Stability of a Star with a Phase Change in General Relativity Theory, Soviet Astronomy 15, 347 (1971).
- [20] B. P. Abbott et al. (LIGO Scientific, Virgo), GW170817: Observation of Gravitational Waves from a Binary Neutron Star Inspiral, Phys. Rev. Lett. 119, 161101 (2017), arXiv:1710.05832 [gr-qc].
- [21] B. P. Abbott et al. (LIGO Scientific, Virgo), GW170817: Measurements of neutron star radii and equation of state, Phys. Rev. Lett. 121, 161101 (2018), arXiv:1805.11581 [gr-qc].
- [22] B. P. Abbott et al. (LIGO Scientific, Virgo), Properties of the binary neutron star merger GW170817, Phys. Rev. X 9, 011001 (2019), arXiv:1805.11579 [gr-qc].

- [23] T. E. Riley and et al., A nicer view of psr j0030+0451: Millisecond pulsar parameter estimation, Astrophysical Journal Letters 887, L21 (2019), arXiv:1912.05702 [astro-ph.HE].
- [24] M. C. Miller and et al., Psr j0030+0451 mass and radius from nicer data and implications for the properties of neutron star matter, Astrophysical Journal Letters 887, L24 (2019), arXiv:1912.05705 [astro-ph.HE].
- [25] V. Doroshenko, V. Suleimanov, G. Pühlhofer, and A. Santangelo, A strangely light neutron star within a supernova remnant, Nature Astronomy 6, 1444 (2022).
- [26] T. E. Riley and et al., A nicer view of the massive pulsar psr j0740+6620 informed by radio timing and xmm-newton spectroscopy, Astrophysical Journal Letters 918, L27 (2021), arXiv:2105.06980 [astro-ph.HE].
- [27] M. C. Miller and et al., The radius of psr j0740+6620 from nicer and xmm-newton data, Astrophysical Journal Letters 918, L28 (2021), arXiv:2105.06979 [astro-ph.HE].
- [28] C. Breu and L. Rezzolla, Maximum mass, moment of inertia and compactness of relativistic stars, Mon. Not.

- Roy. Astron. Soc. **459**, 646 (2016), arXiv:1601.06083 [gr-qc].
- [29] S. Postnikov, M. Prakash, and J. M. Lattimer, Tidal Love Numbers of Neutron and Self-Bound Quark Stars, Phys. Rev. D 82, 024016 (2010), arXiv:1004.5098 [astro-ph.SR].
- [30] J. Takátsy and P. Kovács, Comment on "Tidal Love numbers of neutron and self-bound quark stars", Phys. Rev. D 102, 028501 (2020), arXiv:2007.01139 [astro-ph.HE].
- [31] J. B. Hartle, Slowly rotating relativistic stars. 1. Equations of structure, Astrophys. J. 150, 1005 (1967).
- [32] Z. Hu, X. Miao, and L. Shao, Tests of Classical Gravity with Radio Pulsars, in *Recent Progress on Gravity Tests: Challenges and Future Perspectives* (Springer Nature Singapore, 2024) pp. 61–99, arXiv:2303.17185 [astroph.HE].
- [33] Y. Dong, Z. Hu, R. Xu, and L. Shao, Moment of inertia for axisymmetric neutron stars in the standard model extension, Phys. Rev. D **108**, 104039 (2023), arXiv:2309.02871 [gr-qc].